JOURNAL OF GEOPHYSICAL RESEARCH: PLANETS, VOL. 118, 224–233, doi:10.1002/jgre.20051, 2013

Fault dislocation modeled structure of lobate scarps from Lunar Reconnaissance Orbiter Camera digital terrain models

N. R. Williams,[1] T. R. Watters,[2] M. E. Pritchard,[3] M. E. Banks,[2] and J. F. Bell III[1]

Received 17 September 2012; revised 11 January 2013; accepted 14 January 2013; published 14 February 2013.

[1] Before the launch of the Lunar Reconnaissance Orbiter, known characteristics of lobate scarps on the Moon were limited to studies of only a few dozen scarps revealed in Apollo-era photographs within ~20° of the equator. The Lunar Reconnaissance Orbiter Camera now provides meter-scale images of more than 100 lobate scarps, as well as stereo-derived topography of about a dozen scarps. High-resolution digital terrain models (DTMs) provide unprecedented insight into scarp morphology and dimensions. Here, we analyze images and DTMs of the Slipher, Racah X-1, Mandel'shtam-1, Feoktistov, Simpelius-1, and Oppenheimer F lobate scarps. Parameters in fault dislocation models are iteratively varied to provide best fits to DTM topographic profiles to test previous interpretations that the observed landforms are the result of shallow, low-angle thrust faults. Results suggest that these faults occur from the surface down to depths of hundreds of meters, have dip angles of 35–40°, and have typical maximum slips of tens of meters. These lunar scarp models are comparable to modeled geometries of lobate scarps on Mercury, Mars, and asteroid 433 Eros, but are shallower and ~10° steeper than geometries determined in studies with limited Apollo-era data. Frictional and rock mass strength criteria constrain the state of global differential stress between 3.5 and 18.6 MPa at the modeled maximum depths of faulting. Our results are consistent with thermal history models that predict relatively small compressional stresses that likely arise from cooling of a magma ocean.

Citation: Williams, N. R., T. R. Watters, M. E. Pritchard, M. E. Banks, and J. F. Bell III (2013), Fault dislocation modeled structure of lobate scarps from Lunar Reconnaissance Orbiter Camera digital terrain models, *J. Geophys. Res. Planets, 118*, 224–233, doi:10.1002/jgre.20051.

1. Introduction

[2] Lobate scarps are linear or curvilinear topographic rises that have been observed on all of the terrestrial planets except Venus. To date, lobate scarps have been identified in nearly 100 different locations on the Moon in both the mare and highlands, including over 20 scarps and scarp complexes at latitudes greater than 60° [*Binder and Gunga*, 1985; *Banks et al*., 2012], and appear to be globally distributed [*Watters et al*., 2010]. Lobate scarps are interpreted as shallow, low-angle thrust fault scarps with hanging walls moved up relative to footwalls [*Lucchitta*, 1976; *Binder*, 1982; *Binder and Gunga*, 1985]. Lunar scarps are typically ~10–20 km in length or less, tens to hundreds of meters in width, and up to ~150 m in relief [*Binder and Gunga*, 1985; *Banks et al*., 2012]. In cross section, they appear asymmetric with steep scarp faces (~5–29°), crests typically a few tens of meters high, and gently sloping back limbs [*Binder and Gunga*, 1985; *Watters and Johnson*, 2010; *Banks et al*., 2012]. The vergence direction of many scarps is oriented upslope, but vergence direction sometimes reverses along strike [*Schultz*, 1976]. Scarp complexes or groups often include en echelon stepping segments in parallel or subparallel orientations [*Binder and Gunga*, 1985].

[3] Prior to Lunar Reconnaissance Orbiter (LRO) observations, lobate scarps were only identified in equatorial regions due to limited high-resolution Apollo Panoramic Camera and Lunar Orbiter image coverage with optimal lighting (less than 10% of the lunar surface) [*Binder*, 1982; *Binder and Gunga*, 1985; *Watters and Johnson*, 2010]. Maximum relief of a limited number of lobate scarps was determined with photoclinometry or shadow measurements [*Binder and Gunga*, 1985; *Watters and Johnson*, 2010].

[4] Lobate scarp morphologies are usually crisp and relatively undegraded by impact craters. They are interpreted as some of the youngest endogenic landforms on the Moon, with maximum age estimates of less than 1 billion years based on transected small (<50 m) diameter fresh craters [*Binder and Gunga*, 1985; *Watters et al*., 2010]. The scarps are thought to have formed as a result of late-stage global radial contraction of the Moon [*Binder*, 1982; *Binder and*

[1]School of Earth and Space Exploration, Arizona State University, Tempe, Arizona, USA.
[2]Center for Earth and Planetary Studies, National Air and Space Museum, Smithsonian Institution, Washington, D. C., USA.
[3]Department of Earth and Atmospheric Science, Cornell University, Ithaca, New York, USA.

Corresponding author: N. R. Williams, School of Earth and Space Exploration, Arizona State University, Tempe, AZ 85251, USA. (Nathan.R.Williams@asu.edu).

2169-9097/13/10.1002/jgre.20051

Gunga, 1985; *Watters et al*., 2010; *Watters and Johnson*, 2010]. Radial contraction of the Moon is inferred from the shortening across lobate scarps globally and estimated at ~100 m [*Watters et al*., 2010].

[5] The Hinks Dorsum lobate scarp on asteroid 433 Eros [*Watters et al*., 2011] is comparably sized to lunar scarps, with a maximum relief of 60 m. Lobate scarps on Mercury [*Strom et al*., 1975; *Watters et al*., 2009; *Solomon et al*., 2008] and Mars [*Watters*, 2003], however, can be up to an order of magnitude larger and may have over a kilometer of relief. Fault dislocation models constrained by topographic observations of lobate scarps on Mars, Mercury, and asteroid 433 Eros indicate that the underlying faults are likely planar [*Schultz and Watters*, 2001; *Watters and Schultz*, 2002; *Watters et al*., 2002, 2011]. However, subsurface fault geometries and mechanical properties of the lunar crust and lithosphere remain poorly understood [*Binder and Gunga*, 1985; *Watters and Johnson*, 2010].

[6] Topography derived from Lunar Reconnaissance Orbiter Camera (LROC) stereo images provides new constraints on mechanical and kinematic models for the formation of tectonic landforms on the Moon. Here, morphology and regional context are described for six lunar lobate scarps for which high-resolution LROC stereo images and derived digital terrain models (DTMs) are currently available: Slipher, Racah X-1, Mandel'shtam-1, Feoktistov, Simpelius-1, and Oppenheimer F (informally named for nearby impact craters) (Figure 1). Fault dislocation models are created and compared to DTM topography to constrain the dips, depths, and slip on the faults underlying these lobate scarps. The modeled geometries are then used to constrain the current state of stress in the lunar crust using frictional sliding and cohesive rock failure criteria.

2. Data and Methods

[7] LROC consists of two Narrow-Angle Cameras (NACs) and one Wide-Angle Camera (WAC) [*Robinson et al*., 2010]. From its nominal 50 km altitude orbit, the NACs acquire images with resolutions as high as 50 cm/pix across an approximately 5 km swath, whereas the WAC acquires images with a coarser resolution of ~100 m/pix but a ~104 km wide field of view, providing regional and global context. LROC obtains stereo NAC observations by acquiring at least two NAC images of the same area but from different viewing angles by rolling the spacecraft off-nadir on a subsequent orbit. High-resolution (~2 m/pix, typically 1–3 m vertical precision) DTMs are derived using SOCET-SET software by performing image correlation and edge matching for every pixel in stereo NAC image pairs [*Tran et al*., 2010].

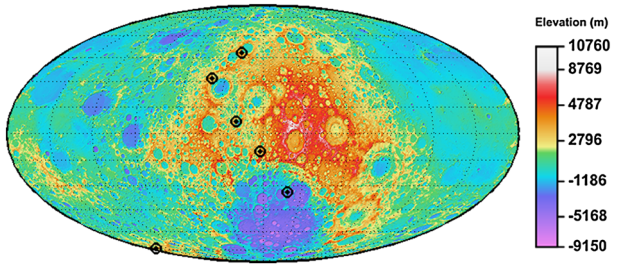

Figure 1. Locations of scarps examined in this study (black circles) overlain on a Mollweide equal area projection map of LROC WAC global 64 pixel per degree topography centered on the anti-Earth point [*Scholten et al*., 2011].

[8] Derived terrain is tied to absolute elevations from Lunar Orbiter Laser Altimeter (LOLA) ranging profiles that cross the scene [*DeVenecia et al*., 2007; *Tran et al*., 2010]. LOLA ranging orbital tracks run approximately north-south with slightly lower horizontal resolutions along-track than LROC NAC stereo-derived DTMs. LOLA ranging has small vertical uncertainties, but can have horizontal uncertainties of 50 and 300 m (with and without crossover analysis, respectively), and tracks typically do not provide continuous coverage along the entire length of the scarp [*Tran et al*., 2010]. LOLA profiles are thus best suited for coarse morphological analyses of east-west trending scarps [*Banks et al*., 2012], while profiles from LROC NAC DTMs can be extracted with any orientation, and where preexisting topographic variations are minimized such that the expression of the scarp is the primary feature in the local topography. For these reasons, we exclusively use NAC stereo-derived DTMs for the analyses in this study. The linear regional slope along each profile is subtracted to detrend and isolate scarp morphology from the surrounding terrain.

[9] Fault dislocation models are created using the Coulomb software package [*Lin and Stein*, 2004; *Toda et al*., 2005] based on stress and material displacement functions for an elastic half-space [*Okada*, 1992]. An elastic modulus (E) of 40 to 80 GPa and Poisson's ratio (ν) of 0.25 are assumed for the lunar crust, comparable to values for Earth's crust [*Turcotte and Schubert*, 2002; *Bürgmann et al*., 1994] and assumed similar for Mercury, Mars, and asteroid 433 Eros [*Schultz and Watters*, 2001; *Watters et al*., 2002; *Watters and Schultz*, 2002; *Watters et al*., 2011]. *Pritchard and Stevenson* [2000] suggest the elastic modulus and Poisson's ratio might be 10–100 times less than normal values because of the heavy impact damage;

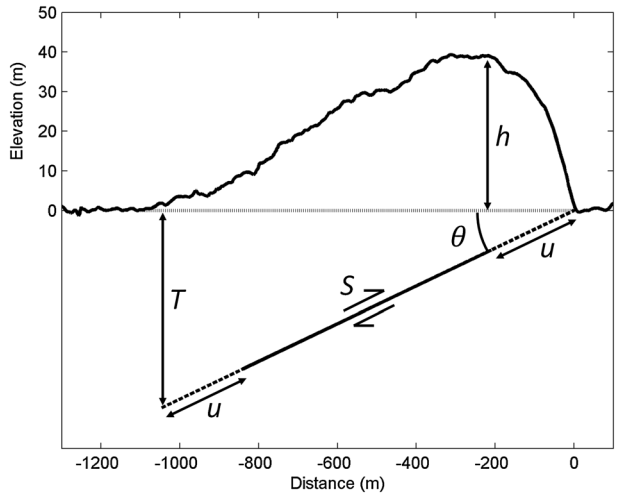

Figure 2. Model parameters for an example lobate scarp profile (Mandel'shtam-1). T is the maximum depth of faulting, h is the maximum relief of the scarp, θ is the fault dip angle, S is the slip, and u is the taper distance where slip decreases from a maximum value of S in the middle of the fault to zero at the tips. The depth of faulting is not to scale.

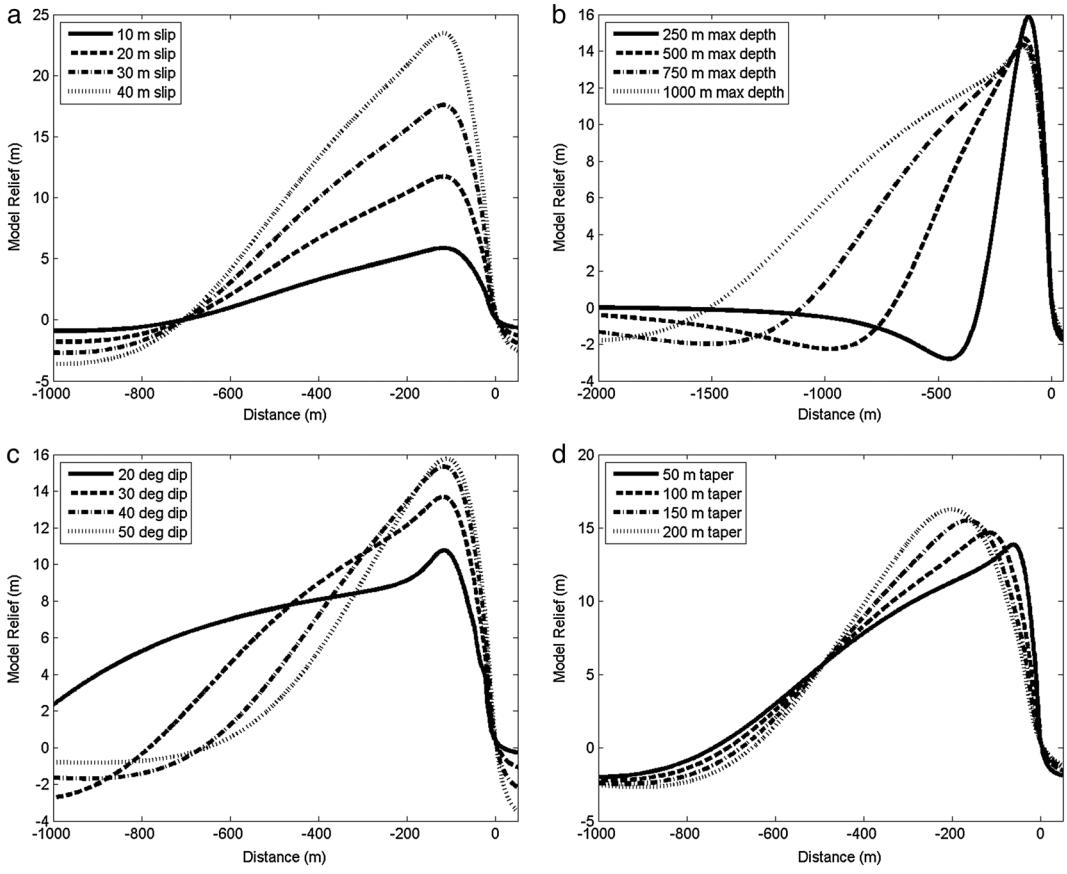

Figure 3a–d. Sensitivity curves for variables in fault dislocation modeling. Unless stated otherwise, fault slip is 25 m, maximum depth is 500 m, dip angle is 35°, and the fault slip is tapered within 100 m of its edges.

however, decreasing these parameters in Coulomb by a factor of 100 has a negligible influence on modeled displacements. Fault geometry and fault slip are the dominant controls of scarp topography. The fault surface is defined as a dipping rectangular plane, suggested for lobate scarp models by *Watters and Schultz* [2002] (Figure 2). The maximum slip S on the fault is first estimated from the maximum relief of the scarp h to provide the vertical scale for a model profile (Figure 3a–da). Maximum depth of faulting T is determined to a first order using the width of the scarp and an approximate fault dip angle (Figure 3a–db). Fault dip angle θ primarily influences the shape of the scarp's back morphology limb, with higher dip angles leading to greater relief in the back limb and eventually creating a hunched back morphology (Figure 3a–dc). Near the edges of the fault plane, slip is allowed to taper from its maximum value to zero in five steps over a distance u from the edge to avoid unrealistically large stress concentrations at the fault tips. Increasing the taper (u) primarily decreases the slope of the scarp face, rounds off the scarp crest, and shifts relief toward the back limb (Figure 3a–dd). Fault dip, depth, slip, and taper are varied iteratively to create forward-modeled profiles with similar relief and slopes to the scarps in the detrended topographic profiles. As discussed below, solutions are nonunique, but suggest narrow ranges for geometric parameters. Fault dislocation models were fit to profiles across the Slipher, Racah X-1, Mandel'shtam-1, Feoktistov, Simpelius-1, and Oppenheimer F lobate scarps. Parameter ranges are determined such that the resulting model does not significantly and consistently deviate (by a value ~20% of the maximum relief over a 100 m baseline) from the detrended profile atop the scarp's face, crest, or back limb, unless the variation in topography is attributed to a landform not associated with deformation on the main scarp, such as an impact crater or a secondary scarp.

[10] The Slipher scarp (48.2°N, 160.8°E) occurs along a bench in the southern wall of the impact crater Slipher (Figures 4a and 5a). The main scarp is oriented E-W with its steepest slope (vergent side) facing south. It also has numerous smaller subparallel scarps that splay or branch off the primary one and sometimes face in the opposite direction (antithetic). A portion of the Slipher scarp also contains small linear graben or troughs superposed on and parallel to the crest of the scarp, possibly indicating localized layer-parallel extension due to flexure of material atop the scarp [*Watters et al*., 2010, 2012]. The main scarp in Slipher is ~20 km long and continues over 100 km east as part of a larger cluster of en echelon stepping scarps along the southern rim of D'Alembert crater. However, high-resolution LROC NAC images are not continuous to the east of D'Alembert crater, so the scarp's full extent has not yet been determined. Its maximum detrended relief within Slipher crater has been measured as ~21 m [*Banks et al*., 2012], but may be greater in the D'Alembert section.

[11] The Racah X-1 scarp (10.1°S, 178.1°E) has the largest maximum relief (~150 m) of any lunar lobate scarps measured to date [*Banks et al*., 2012] (Figures 4b and 5b).

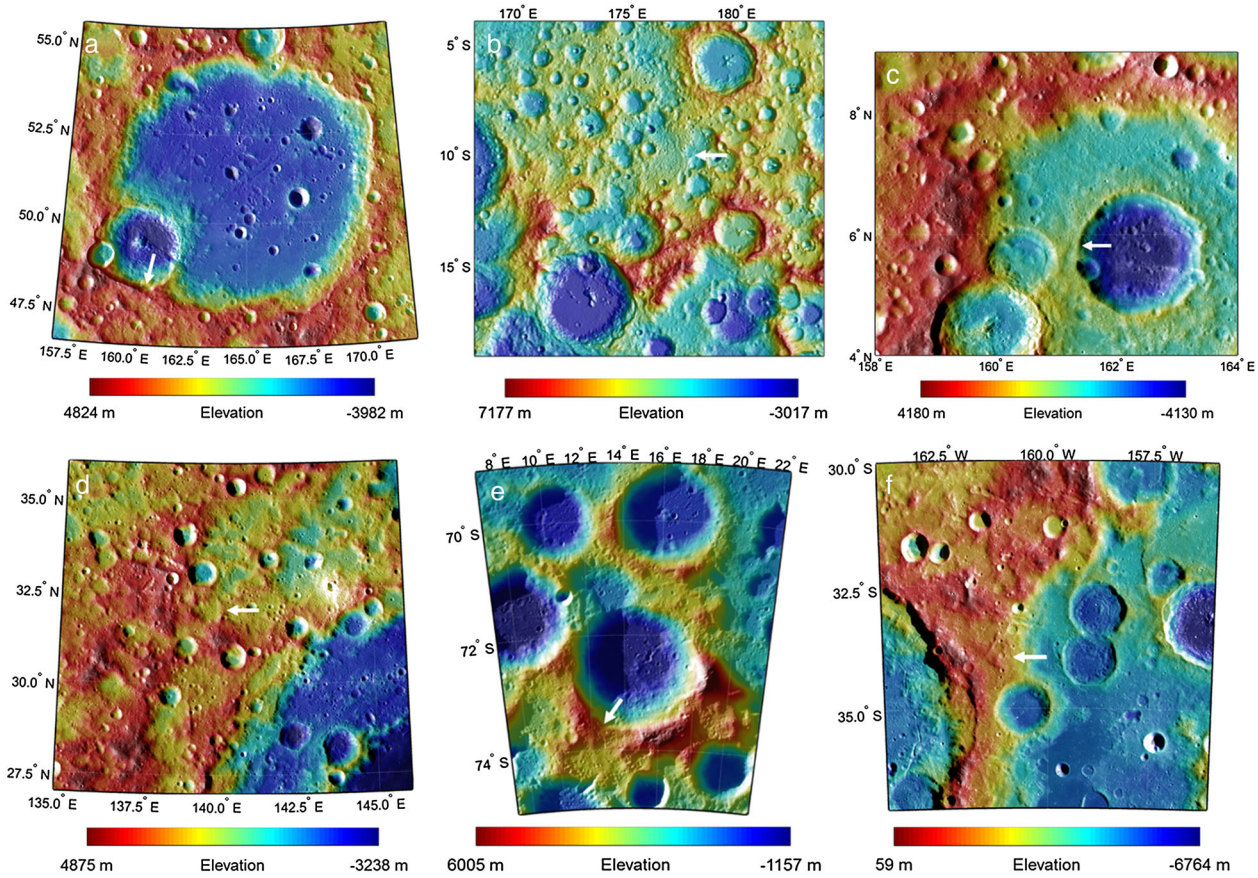

Figure 4. LROC WAC colorized shaded relief mosaics [*Scholten et al*., 2011] of (a) Slipher, (b) Racah X-1, (c) Mandel'shtam-1, (d) Feoktistov, (e) Simpelius-1, and (f) Oppenheimer F. White arrows point to the locations of scarps examined in this study.

The main scarp cuts across several tens of kilometers of undulating, densely cratered highland terrain, making characterization of its morphology difficult. Several en echelon scarps continue farther north of the DTM coverage up to and into Daedalus crater. At its northern end, the scarps transition into more complex wrinkle ridges on the flat floor of Daedalus. Such a morphologic transition is likely due to the contrast in mechanical properties, especially the presence of layering in mare basalts in Daedalus [*Watters*, 1991]. The en echelon complex also continues southward from the DTM area toward the Aitken crater. Scarps in the Racah X complex typically trace N-S, with the main scarp face (vergent side) and many other segments oriented eastward. Like Slipher, small flat-floored troughs are present near and atop the Racah X-1 scarp [*Banks et al*., 2012].

[12] The Mandel'shtam-1 lobate scarp (5.86°N, 161.49°E) was first identified in Apollo Panoramic Camera images (Figures 4c and 5c) [*Binder and Gunga*, 1985]. It is one member of an arcuate scarp complex in Mandel'shtam crater starting in Mandel'shtam A crater and continuing 80 km north along the floor of Mandel'shtam. Scarps in this cluster typically trace N-S with scarp faces oriented westward. Maximum detrended relief of the Mandel'shtam-1 scarp is measured in the DTM at ~38 m. Some portions of the scarp face are terraced, indicating possible splay faults at each end.

[13] The Feoktistov scarp (32°N, 140.6°E) is located in the highlands north of the small crater Feoktistov and approximately 60 km northwest of the outer rim of Mare Moscoviense (Figures 4d and 5d). The main scarp trace appears braided and has a few antithetic scarps, indicating that the fault splays near the surface. The main scarp trends N-S with the vergent side of the scarp oriented to the west. A small cluster of meter-scale troughs or graben occur in the hanging wall near the middle of the scarp and are oriented at a high angle to the scarp face. The maximum relief of Feoktistov within the DTM is ~22 m, measured near the scarp's southern terminus.

[14] Simpelius-1 (73.5°S, 13°E) is a cluster of relatively small, kilometer long, low-relief scarps on the wall and floor of the south side of Simpelius crater (Figures 4e and 5e). The southern portion of the scarp cluster is covered by the available DTM and traces E-W along the wall of Simpelius crater. The vergent side of the scarp faces uphill to the south. Its maximum relief is approximately 13 m within the portion covered by the DTM [*Banks et al*., 2012].

[15] Finally, Oppenheimer F (34°S, 160.9°W) is a simple en echelon complex of parallel linear scarps located north of the Oppenheimer F crater (Figures 4f and 5f). The scarps trend NNE-SSW along the degraded outer rim of Apollo crater on the northern side of the South Pole–Aitken basin. The vergent sides of the scarps face to the west. Typical

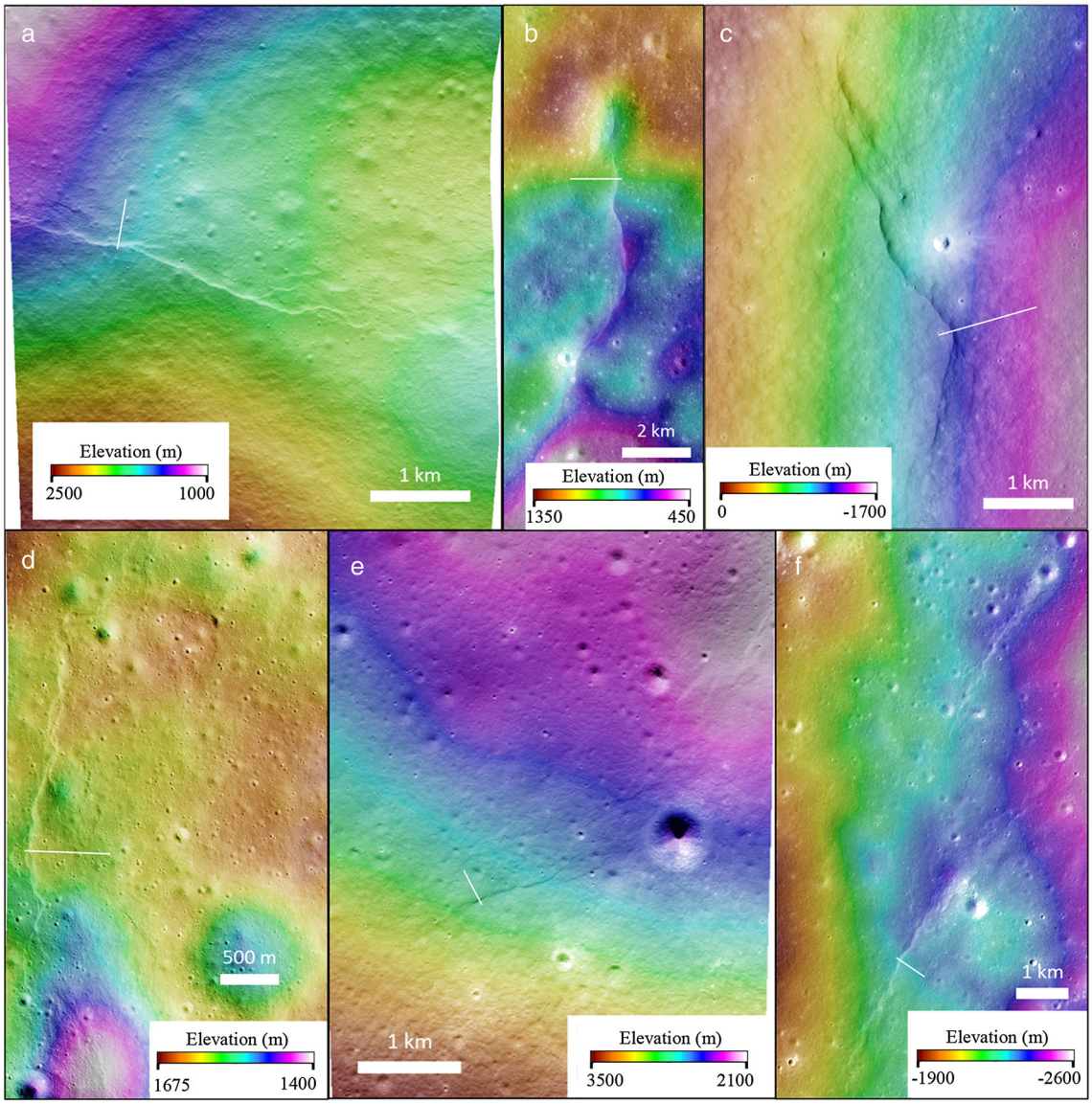

Figure 5. LROC NAC DTM colorized shaded relief images of (a) Slipher, (b) Racah X-1, (c) Mandel'shtam-1, (d) Feoktistov, (e) Simpelius-1, and (f) Oppenheimer F. Profiles from Figure 6 were taken along locations indicated by narrow white lines.

lengths of individual scarps are less than 5 km, and the en echelon complex of scarps continues for at least 60 km before continuous NAC image coverage ends.

3. Modeling Results

[16] Profiles across representative sections of each scarp were extracted from NAC stereo-derived DTMs. Faults are interpreted to dip from the base of a scarp face downward under the gently sloping back limb. Coulomb fault dislocation models were iteratively created and compared to detrended profiles (Figure 6) to determine sets of parameter values that predict similar scarp reliefs and slopes. Parameter ranges for each scarp profile are listed in Table 1. Best fit dip angles range from 35° to 40°, depths range from 220 to 900 m, taper increments (for five steps) range from 50 to 250 m, and slips range from 18 to 62 m along the profiles modeled. Fault geometry is therefore dominant in controlling scarp topography.

[17] These ranges of lunar lobate scarp fault dips also constrain previous estimates of horizontal shortening across lunar lobate scarps. *Banks et al*. [2012] determined reliefs of scarps globally range from ~5 to 150 m, and assuming dip angles of 20–40°, predicted individual scarps may accommodate up to ~410 m of horizontal shortening. Lower limits of horizontal shortening (S_H) can be calculated via a simple kinematic model using measured maximum scarp reliefs (h) and fault plane dip angles (θ) [*Wojtal*, 1996; *Watters and Robinson*, 1999; *Watters et al*., 2000]:

$$S_H = h/\tan(\theta). \quad (1)$$

[18] Using a maximum measured scarp relief of 150 m [*Banks et al*., 2012] and our modeled range of fault plane

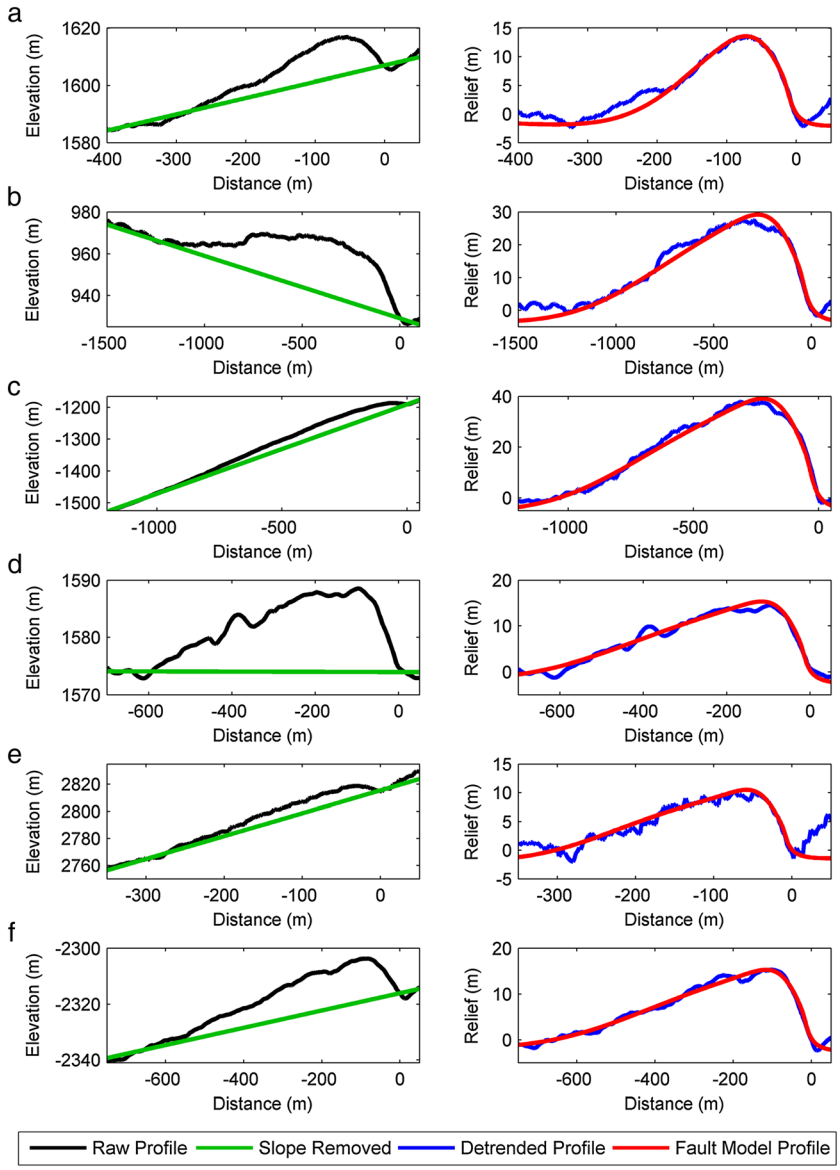

Figure 6. Raw profiles, regional slopes removed, detrended profiles, and best fit fault dislocation models for profiles of (a) Slipher, (b) Racah X-1, (c) Mandel'shtam-1, (d) Feoktistov, (e) Simpelius-1, and (f) Oppenheimer F.

dip angles of 35–40°, we estimate horizontal shortening of up to 215 m across individual lunar lobate scarps, nearly half of the up to ~410 m shortening estimated by *Banks et al.* [2012] using smaller fault plane dip angles.

4. Stress State

[19] The presence of a global population of near-surface faults on the Moon constrains the current state of lunar lithospheric stress [*Binder and Gunga*, 1985; *Watters et al.*, 2010]. The compressional stress necessary to initiate thrust faulting can be determined by the Moon's near-surface strength. At least two approaches can be used to evaluate the near-surface shear strength of the lunar crust: frictional and rock mass criteria. Frictional strength is controlled by the resistance to brittle failure by sliding on randomly oriented, throughgoing fractures. Such fractures are likely in the heavily impacted upper crust of the Moon. The minimum horizontal stress required to initiate faulting can be given by the following:

$$\Delta\sigma_{xx} = (2{\cdot}\mu_s{\cdot}(\rho{\cdot}g{\cdot}z - p_w))/\left(\left(1+\mu_s{}^2\right)^{1/2} - \mu_s\right), \qquad (2)$$

where μ_s is the coefficient of static friction, ρ is the average rock density, g is gravitational acceleration, z is depth, and

Table 1. Best Fit Model Parameter Results for Profiles Across Scarps

Scarp	Slip (m)	Dip (°)	Depth (m)	Five-step taper increment (m)
Slipher	21 ± 1	38 ± 2	250 ± 50	75
Racah X-1	45 ± 2	38 ± 3	900 ± 50	250
Mandel'shtam-1	62 ± 3	37 ± 2	770 ± 25	200
Feoktistov	25 ± 2	40 ± 4	500 ± 50	100
Simpelius-1	18 ± 2	35 ± 3	220 ± 25	50
Oppenheimer F	25 ± 2	40 ± 3	500 ± 50	100

p_w is the pore pressure, which for the Moon is zero [*Turcotte and Schubert*, 2002]. The coefficient of static friction μ_s is estimated to be 0.85 by the empirical fit known as Byerlee's law [*Byerlee*, 1978]. Using a density (ρ) of 2700 kg/m^3 and gravitational acceleration (g) of 1.624 m/s^2 [*Binder and Gunga*, 1985], we estimate the minimum frictional strength ($\Delta\sigma_{xx}$) in rock exceeded at modeled depths from 220 and 900 m to be between 3.5 and 14.5 MPa (Figure 7).

[20] The frictional strength criterion assumes rocks have no cohesive strength, so it should be regarded as a minimum stress requirement. Rocks with cohesive strength may be better represented by the Hoek-Brown failure criteria [*Hoek*, 2001; *Hoek et al*., 2002; *Hoek and Diederichs*, 2006]:

$$\sigma_1 = \sigma_3 + \sigma_{ci}\cdot(m_b\cdot\sigma_3/\sigma_{ci} + s)^a, \tag{3}$$

$$\Delta\sigma_{xx} = \sigma_1 - \sigma_3, \tag{4}$$

such that σ_1 is the greatest compressional principal effective stress, σ_3 is the least compressional principal effective stress, σ_{ci} is the intact rock strength, and m_b, m_i, a, and s are material constants related to the Geological Strength Index (GSI) and the disturbance factor d by

$$m_b = m_i\cdot e^{(GSI-100)/(28-14d)}, \tag{5}$$

$$s = e^{(GSI-100)}/(9-3d), \tag{6}$$

$$a = {}^1/_2 + \left(e^{-GSI/15} - e^{-20/3}\right)/6. \tag{7}$$

[21] Using GSI = 45 consistent with highly jointed rock mass [*Hoek et al*., 2002; *Watters et al*., 2011]; σ_{ci} = 190 MPa as an upper limit for anorthosite [*Hustrulid and Bullock*, 2001] consistent with the 100–250 MPa expected for a typical very good quality hard rock mass [*Hoek et al*., 2001] medium-textured felsic igneous rock m_i = 25 [*Hoek et al*., 2001] and disturbance factor d = 1.0 (where 0 is undisturbed and 1 is very disturbed/heavily fractured) [*Hoek et al*., 2002], the cohesive rock mass strength ($\Delta\sigma_{xx}$) exceeded at 220 and 900 m depth is between 9.2 and 18.6 MPa.

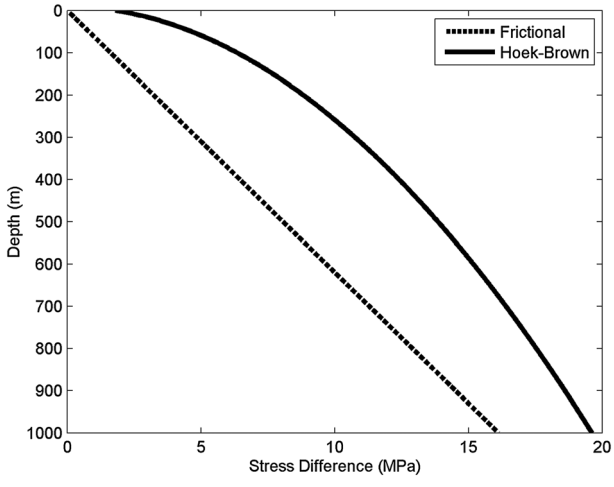

Figure 7. Strength envelopes for the shallow lunar subsurface. The frictional strength envelope was determined using the method described in *Turcotte and Schubert* [2002]. The Hoek-Brown strength envelope for nonzero cohesion was determined with material constants consistent with a highly disturbed anorthosite.

5. Discussion

[22] All six scarp models are consistent with deformation from thrust faulting at typical dip angles of 35–40° and maximum faulting depths from a few hundred meters to around a kilometer. *Binder and Gunga* [1985] previously used Apollo image photoclinometry, shadow measurements, and half-angles of scarp trace curvature for inferred conical (arcuate) faults to estimate dip angles for observed lunar lobate scarps at 17–30° (with an average of 21.4°) and maximum depths of 400 m to 3.8 km. Additionally, their scaled sandbox experiments suggested dip angles of 25° and maximum depths of 1–8 km based on an arcuate thrust fault theory. Curvature of scarp traces is common, but not ubiquitous on the Moon. For example, the traces of the Slipher and Oppenheimer F scarps are not arcuate, yet their morphology suggests a fault geometry similar to other scarps. Our modeled thrust fault dips (35–40°) are steeper and our modeled depths (less than 1 km) are shallower, but do not assume an arcuate fault geometry unrepresentative of the many linear or irregular lobate scarps traces [*Binder and Gunga*, 1985; *Watters et al*., 2010; *Banks et al*., 2012]. Our model results also fit reliefs and slopes of the scarp face, crest, and back limb instead of only maximum height.

[23] The subkilometer depths we modeled for lunar lobate scarp faults, as opposed to more deeply rooted faults that extend to greater depths, suggest that they may be restricted to weaker near-surface materials. *Wilcox et al*. [2005] show that regolith occurs above an uneven, undulating fractured bedrock surface that grades up toward the surface with decreasingly cohesive material, perhaps on the order of hundreds of meters to kilometers. We infer that the megaregolith layer is weak enough for faults to grow within the upper few hundred meters to a kilometer at stresses of 3.5–18.6 MPa. Areas with the most pervasive fracturing, such as near large craters, might facilitate faulting due to decreased rock strength [*Sharpton and Head*, 1988]. Scarps analyzed in this study occur both in association with craters and in the highlands and variations in location and geologic setting do not appear to have a significant influence on the results [*Binder and Gunga*, 1985; *Watters et al*., 2010]. At greater depths, material strength of the megaregolith or bedrock may be great enough that the current stress state is insufficient to allow for deeper fault propagation into a more coherent upper portion of the elastic lithosphere.

[24] Lobate scarps also occur on other planetary bodies and have previously been modeled with geometries similar to our lunar scarp models. The lobate scarp Hinks Dorsum on asteroid 433 Eros has approximately 60 m of maximum relief, and its subsidiary scarps have maximum reliefs of 25 m [*Watters et al*., 2011]. Fault dislocation models suggest that the main Hinks Dorsum fault has a dip of ~40°, maximum depth of 240 m, and a fault slip of ~90 m. Scarps subsidiary to Hinks Dorsum have modeled dips of ~35°, maximum depth of ~200 m, and slip of ~40 m [*Watters et al*., 2011]. The subsurface geometries of Hinks Dorsum and its subsidiary scarps fall within the range of values estimated for the lunar lobate scarps modeled in our study.

Using equation (1) and the relief and dip values from *Watters et al*. [2011], we estimate 30–71.5 m of horizontal shortening for scarps on 433 Eros, also within the range we estimate for lunar lobate scarps. Eros' scarps are interpreted to have formed by compressional stresses during or shortly after a large nearby impact that formed a ~7.6 km diameter crater [*Watters et al*., 2011]; however, lunar lobate scarps do not appear to be associated with recent large impacts. Although the sources of stress are almost certainly different for lunar scarps versus those on Eros, the similar model geometries suggest that stress magnitudes and some material properties of the regoliths (i.e., coefficient of static friction) on both bodies may be similar.

[25] Lobate scarps on Mars and Mercury have maximum reliefs of up to a kilometer or more, but show similar morphologies to lunar scarps. *Watters and Schultz* [2002] created fault dislocation models for Discovery Rupes on Mercury and Amenthes Rupes on Mars using listric fault geometries with dips that shallow with increasing depth; however, only a slight or no curve (±5°) in the fault fits the observed topography, planar faults fit best, and décollement models with dips that that shallow to nearly horizontal fit poorest. The best fit geometry of the Mercurian Discovery Rupes is a 30–35° dip with a maximum depth of 35–40 km and a fault slip of 2.2 km [*Watters and Schultz*, 2002; *Watters et al*., 2002]. The best fit geometry of the Martian Amenthes Rupes is a 30° dip with a maximum depth of 25 km and a fault slip of 1.6 km [*Schultz and Watters*, 2001]. Due to order of magnitude smaller fault slips predicted for lunar scarps compared to those on Mars and Mercury, maximum depths of faulting are expected to be much shallower on the Moon, consistent with the model results presented above. However, the modeled dips of the Mercurian and Martian lobate fault scarps are comparable to lunar fault scarp models within ±5°.

[26] The amounts of global radial contraction inferred from larger scarp populations on Mercury and Mars are similarly an order of magnitude greater than contraction estimates for the Moon. Previous studies have estimated the change in radius for Mercury to be at least 0.8 km [e.g., *Watters et al*., 1998, 2009; *Watters and Nimmo*, 2010] and for Mars to be between 112 m and 3.77 km [e.g., *Mangold et al*., 2000; *Golombek et al*., 2001; *Golombek and Phillips*, 2010; *Nahm and Schultz*, 2011]. The smaller magnitudes of slip and relief we find for lobate scarps on the Moon are consistent with recent estimates of lunar radial contraction of ~100 m [*Watters et al*., 2010; *Banks et al*., 2012].

[27] The small but significant compressional strain across the global population of lunar lobate scarps is thought to be due to heat loss and planetary thermal contraction over the Moon's history [*Binder and Gunga*, 1985; *Pritchard and Stevenson*, 2000; *Watters et al*., 2010]. The lack of a latitude or longitude dependence on lobate scarps suggests that the Moon is in a state of net (perhaps isotropic) contraction. Relaxation of an early tidal bulge or tidal stresses raised solely by Earth would be predominantly extensional near the poles and compressional around the sub-Earth and anti-Earth regions [*Melosh*, 1980]. Such a pattern is not observed, but tidal stresses may still play a secondary role in scarp formation (i.e., influencing preferred orientation) [*Watters et al*., 2010]. Tidal stress raised solely by Earth would also only be on the order of tens of kilopascals [*Weber et al*., 2009], too low to initiate faulting by itself in 3.5–18.6 MPa strength material [*Watters et al*., 2010; *Banks et al*., 2012; *Turcotte and Schubert*, 2002; this study].

[28] Crater counts of mare basins crosscut by large-scale graben indicate that basin-related extension occurred before ~3.6 Ga [*Lucchitta and Watkins*, 1978; *Solomon and Head*, 1979]. Turning off of large-scale extension may result from superposition of increasing global contractional stresses via cooling, leading to a predominantly compressional regime thereafter [*Solomon and Head*, 1979]. Over the last ~3.5 Ga, global stresses would build and may have only exceeded rock mass strengths of 3.5–18.6 MPa in the geologically recent past, potentially explaining why lunar lobate scarps have ubiquitously fresh, crisp morphologies consistent with recent (<1 Ga) activity [*Binder and Gunga*, 1985; *Watters et al*., 2010]. Recently discovered young (<50 Ma) small-scale shallow graben on the lunar surface are consistent with localized extensional stresses of about 12 MPa in the presence of a low ~10 MPa background compressional stress, which may be relaxed by the formation of associated scarps where near-surface flexure results in extension in the area of the scarp back limb [*Watters et al*., 2012]. The presence of young graben in the back limb terrain suggests that some scarp deformation may be concurrent with shallow graben formation as recently as 50 Ma and could possibly even continue today.

[29] If the Moon was initially completely molten, radial contraction from cooling could be expected to have been on the order of a kilometer or more with stresses up to 350 MPa [*Binder and Lange*, 1980; *Binder*, 1982; *Binder and Gunga*, 1985; *Binder*, 1986; *Pritchard and Stevenson*, 2000]. Our estimated 3.5–18.6 MPa of compressional stress necessary to initiate thrust faulting at the modeled depths (220 and 900 m, respectively) are consistent with thermal history models that predict small but significant global net compressional stresses (<100 MPa) that could arise from an initially hot exterior magma ocean superposed on a cooler interior [*Solomon and Chaiken*, 1976; *Solomon and Head*, 1979; *Solomon and Head*, 1980; *Kirk and Stevenson*, 1989; *Pritchard and Stevenson*, 2000]. The shallow faulting we model, which does not penetrate deeper into more coherent rock, further implies a low stress state consistent with only a small amount (~100 m) of net radial contraction of the Moon estimated from the global scarp population [*Binder and Gunga*, 1985; *Watters et al*., 2010].

6. Summary and Conclusions

[30] We performed fault dislocation modeling using LROC NAC DTMs for six lunar lobate scarps to determine their fault geometries. The six scarp models are consistent with deformation from thrust faulting at typical dip angles of 35–40° and maximum faulting depths from a few hundred meters to around a kilometer. Although a subset of the global population of lobate scarps was used in this study, their morphology is characteristic of other scarps [*Banks et al*., 2012]. Since fault geometry is the principal variable in controlling lobate scarp topography, we expect other scarps to have similar fault geometries. Our model fault dips are steeper and have shallower maximum depths than Apollo-era estimates, but are comparable to other fault dislocation models created for lobate scarps on asteroid

433 Eros [*Watters et al*., 2011] and larger scarps on Mercury [*Watters and Schultz*, 2002; *Watters et al*., 2002] and Mars [*Schultz and Watters*, 2001]. Based on modeled depths of faulting, we estimate between 3.5 and 18.6 MPa of differential stress within a kilometer of the lunar surface at the time of faulting. This low level of compressional stress needed to initiate shallow-rooted thrust faults on the Moon is consistent with thermal history models that predict a relatively small amount of late-stage stress from global radial contraction.

[31] **Acknowledgments.** We gratefully acknowledge Mark Robinson, Thanh Tran, and the rest of the LRO and LROC teams. We also acknowledge the constructive comments of the two anonymous reviewers and the Associate Editor. This work was supported by the LRO Project, Arizona State University School of Earth and Space Exploration, Smithsonian Institution National Air and Space Museum, and the Cornell University College of Engineering.

References

Banks, M. E., T. R. Watters, M. S. Robinson, L. L. Tornabene, T. Tran, L. Ojha, and N. R. Williams (2012), Morphometric analysis of small-scale lobate scarps on the Moon using data from the Lunar Reconnaissance Orbiter, *J Geophys Res*, *117*, doi:10.1029/2011JE003907.

Binder, A. B., and M. A. Lange (1980), On the thermal history of the Moon of fission origin, *Moon*, *17*, 29–45.

Binder, A. B. (1982), Post-Imbrian global lunar tectonism: Evidence for an initially totally molten Moon, *Moon Planets*, *26*, 117–133.

Binder, A. B., and H.-C. Gunga (1985), Young thrust-fault scarps in the highlands: Evidence for an initially totally molten Moon, *Icarus*, *63*, 421–441.

Binder, A. B. (1986), The initial thermal state of the Moon, in Origin of the Moon, pp. 425–433, Lunar and Planetary Institute.

Bürgmann, R., D. D. Pollard, and S. J. Martel (1994), Slip distributions on faults: Effects of stress gradients, inelastic deformation, heterogeneous host rock stiffness, and fault interaction, *J. Struct. Geol.*, *16*, 1675–1690.

Byerlee, J. D. (1978), Friction of rocks, *Pure Appl. Geophys.*, *116*, 615–626.

DeVenecia, K., A. S. Walker, and B. Zhang (2007), New approaches to generating and processing high resolution elevation data with imagery, in Photogrammetric Week 2007, edited by D. Fritsch, pp. 297–308, Wichmann, Heidelberg.

Golombek, M. P., F. S. Anderson, and M. T. Zuber (2001), Martian wrinkle ridge topography: Evidence for subsurface faults from MOLA, *J Geophys Res 106*, 23,811–23,821.

Golombek, M. P., and R. J. Phillips (2010), Mars tectonics, in Planetary Tectonics, edited by T. R. Watters, and R. A. Schutlz, pp. 183–232, Cambridge University Press.

Hoek, E. (2001), Rock mass properties for underground mines, in *Underground Mining Methods: Engineering Fundamentals and International Case Studies*, edited by W. A. Hustrulid and R. L. Bullock, Society for Mining, Metallurgy, and Exploration, Littleton, Colo.

Hoek, E., C. Carranza-Torres, and B. Corkum (2002), Hoek-Brown failure criterion, in *Proceedings 5th North American Rock Mechanics Symposium*, edited by R. P. Young, pp. 267–273, Toronto, Ont., Canada.

Hoek, E., and M. S. Diederichs (2006), Empirical estimation of rock mass modulus, *Int. J. Rock Mech. Min. Sci.*, *43*, 203–215, doi:10.1016/j.ijrmms.2005.06.005.

Hustrulid, W. A., and R. L. Bullock (2001), Underground Mining Methods—Engineering Fundamentals and International Case Studies, 305 pp., Society for Mining, Metallurgy, and Exploration.

Kirk, R. L., and D. J. Stevenson (1989), The competition between thermal contraction and differentiation in the stress history of the Moon, *J Geophys Res*, *94*, 12,133–12,144.

Lin, J., and R. S. Stein (2004), Stress triggering in thrust and subduction earthquakes, and stress interaction between the southern San Andreas and nearby thrust and strike-slip faults, *J Geophys Res 109*, B02303, doi:10.1029/2003JB002607.

Lucchitta, B. K. (1976), Mare ridges and related highland scarps: results of vertical tectonism, in *Proceedings of the 7th Lunar and Planetary Science Conference*, pp. 2761–2782.

Lucchitta, B. K., and J. A. Watkins (1978), Large grabens and lunar tectonism, in *Proceedings of the 9th Lunar and Planetary Science Conference*, pp. 666–668.

Mangold, N., P. Allemand, P. G. Thomas, and G. Vidal (2000), Chronology of compressional deformation on Mars: Evidence for a single and global origin, *Planet. Space Sci.*, *48*, 1201–1211.

Melosh, H. J. (1980), Tectonic patterns on a tidally distorted planet, *Icarus*, *43*, 334–337.

Nahm, A. L., and R. A. Schultz (2011), Magnitude of global contraction on Mars from analysis of surface faults: Implications for Martian thermal history, *Icarus*, *211*, 389–400.

Okada, Y. (1992), Internal deformation due to shear and tensile faults in a half-space, *Bull Seismol Soc Am*, *82*, 1018–1040.

Pritchard, M. E., and D. J. Stevenson (2000), Thermal aspects of a lunar origin by giant impact, in Origin of the Earth and Moon, pp. 179–196, University of Arizona Press.

Robinson, M. S., et al. (2010), Lunar Reconnaissance Orbiter Camera (LROC) instrument overview, *Space Sci. Rev.*, *150*, 81–124.

Scholten, F., J. Oberst, K.-D. Matz, T. Roatsch, M. Wählisch, M. S. Robinson, and the LROC Team (2011), GLD100—The Global Lunar 100 Meter Raster DTM from LROC WAC stereo models, in *Proceedings of the 42nd Lunar and Planetary Science Conference*, p. 2046.

Schultz, P. H. (1976), Moon Morphology: Interpretations based on Lunar Orbiter Photography , p. 626, University of Texas Press, Austin, Tex.

Schultz, R. A., and T. R. Watters (2001), Forward mechanical modeling of the Amenthes Rupes thrust fault on Mars, *Geophys Res Lett*, *28*, 4659–4662.

Sharpton, V. L., and J. W. Head (1988), Lunar mare ridges: Analysis of ridge-crater intersections and implications for the tectonic origin of mare ridges, in *Proceedings of the 18th Lunar and Planetary Science Conference*, pp. 307–317.

Solomon, S. C., and J. Chaiken (1976), Thermal expansion and thermal stress in the Moon and terrestrial planets: Clues of early thermal history, in *Proceedings of the 7th Lunar and Planetary Science Conference*, pp. 3229–3243.

Solomon, S. C., and J. W. Head (1979), Vertical movement in mare basins: Relation to mare emplacement, basin tectonics, and lunar thermal history, *J Geophys Res*, *84*, 1667–1682.

Solomon, S. C., and J. W. Head (1980), Lunar mascon basins: Lava filling, tectonics, and evolution of the lithosphere, *Rev. Geophys. Space Phys.*, *18*, 107–141.

Solomon, S. C., et al. (2008), Return to Mercury: A global perspective on MESSENGER's first Mercury flyby, *Science*, *321*, 59, doi:10.1126/science.1159706.

Strom, R. G., N. J. Trask, and J. E. Guest (1975), Tectonism and volcanism on Mercury, *J Geophys Res*, *80*, 2478–2507.

Toda, S., R. S. Stein, K. Richards-Dinger, and S. Bozkurt (2005), Forecasting the evolution of seismicity in southern California: Animations built on earthquake stress transfer, *J Geophys Res* B05S16, doi:10.1029/2004JB003415.

Tran, T., et al. (2010), Generating Digital Terrain Models Using LROC NAC Images, ASPRS/CaGIS Specialty Conference.

Turcotte, D. L., and G. Schubert (2002), *Geodynamics: Application of Continuum Physics to Geological Problems*, 2nd ed., 450 pp., John Wiley, New York.

Watters, T. R. (1991), Origin of periodically space wrinkle Ridges on the Tharsis Plateau of Mars, *J Geophys Res*, *96*, 15,599–15,616.

Watters, T. R., M. S. Robinson, and A. C. Cook (1998), Topography of lobate scarps on Mercury: New constraints on the planet's contraction, *Geology*, *26*, 991–994.

Watters, T. R., and M. S. Robinson (1999), Lobate scarps and the Martian crustal dichotomy, *J Geophys Res*, *104*, 18981–18990.

Watters, T. R., R. A. Schultz, and M. S. Robinson (2000), Displacement-length relations of thrust faults associated with lobate scarps on Mercury and Mars: Comparison with terrestrial faults, *Geophys Res Lett*, *27*, 3659–3662.

Watters, T. R., R. A. Schultz, M. S. Robinson, and A. C. Cook (2002), The mechanical and thermal structure of Mercury's early lithosphere, *Geophys Res Lett*, *29*, doi:10.1029/2001GL014308.

Watters, T. R., and R. A. Schultz (2002), The fault geometry of planetary lobate scarps: Listric versus planar, *Proceedings of the 33rd Lunar and Planetary Science Conference*, Abs. 1668.

Watters T. R. (2003), Thrust faults along the dichotomy boundary in the eastern hemisphere of Mars, *J Geophys Res 108*, doi:10.1029/2002JE001934.

Watters, T. R., S. C. Solomon, M. S. Robinson, J. W. Head, S. L. André, S. A. Hauck II, and S. L. Murchie (2009), The tectonics of Mercury: The view after MESSENGER's first flyby, *Earth Planet. Sci. Lett.*, *285*, 283–296.

Watters, T. R., et al. (2010), Evidence of recent thrust faulting on the Moon revealed by the Lunar Reconnaissance Orbiter Camera, *Science*, *329*, 936–940.

Watters, T. R., and C. L. Johnson (2010), Lunar tectonics, in Planetary Tectonics, edited by T. R. Watters, and R. A. Schutlz, pp. 121–182, Cambridge University Press.

Watters, T. R., and F. Nimmo (2010), The tectonics of Mercury, in Planetary Tectonics, edited by T. R. Watters, and R. A. Schutlz, pp. 15–80, Cambridge University Press.

Watters, T. R., P. C. Thomas, and M. S. Robinson (2011), Thrust faults and the near-surface strength of asteroid 433 Eros, *Geophys Res Lett 38*, L02202, doi:10.1029/2010GL045302.

Watters, T. R., M. S. Robinson, M. E. Banks, T. Tran, and B. W. Denevi (2012), Recent extensional tectonics on the moon revealed by the Lunar Reconnaissance Orbiter Camera, *Nat Geosci*, doi: 10.1038/NGEO1387.

Weber, R. C., B. G. Bills, and C. L. Johnson (2009), Constraints on deep moonquake focal mechanisms through analyses of tidal stress, *J Geophys Res*, *114*, E05001.

Wilcox, B. B., M. S. Robinson, P. C. Thomas, and B. R. Hawke (2005), Constraints on the depth and variability of the lunar regolith, *Meteorit. Planet. Sci.*, *40*, 695–710.

Wojtal, S. F. (1996), Changes in fault displacement populations correlated to linkage between faults, *J. Struct. Geol.*, *18*, 265–279, doi:10.1016/S0191-8141(96)80049-6.